Graphene-Based Epoxy Resin Application on Laminated Composite Materials for Aeronautical Structures

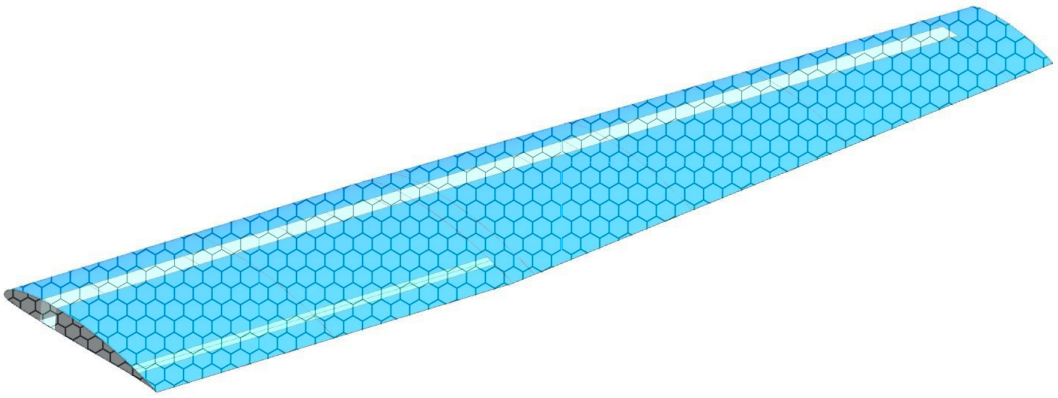

Author: ALFAL/ENGAER 139925-L António Luís Monteiro Oliveira
Master of Science Degree in Military and Aeronautical Sciences – Aeronautical Engineering
Academia da Força Aérea, Sintra

Supervisor: TCOR/ENGAER 129905-A Luís Filipe da Silva Félix
Centro de Investigação da Academia da Força Aérea
Academia da Força Aérea, Sintra

Co-Supervisor: Rui P.F.F. da Silva
MSc in Chemical Engineering
CTO @ Graphenest S.A., Sever do Vouga

Abstract

Graphene is a recent material whose properties allow it to replace or complement other materials in various applications. Given its high rigidity, it opens the door for its use in aeronautical structures, which apart from having their mechanical properties improved, it also allows for weight reduction of such structures.

The main objective of this work is to characterize laminated composite materials made of three different matrices, in order to evaluate the impact that graphene has on the mechanical properties of laminates. The implementation of graphene in aeronautical structures is also studied, specifically, in the design of a wing structure for a class I unmanned aerial vehicle ($<$ 25 kg).

Initially, tensile and bending tests were carried out with specimens manufactured with three different matrices: the matrix used at the *Centro de Investigação da Academia da Força Aérea*; the graphene-based matrix produced by Graphenest, S.A.; and the base matrix used in the production of the previous one, but without graphene. Tests were carried out with bidirectional and unidirectional carbon fibers until material failure occurred. Improvements of 6.2% in the modulus of elasticity between the graphene matrix and the first one were obtained.

Finally, the obtained properties were implemented on the wing design, using finite element analysis. Linear static and linear buckling analyses were performed, and decreases of 0.6% to 6.2% in stress and 6.1% in displacement were obtained, when comparing the graphene-based matrix with the first one.

Keywords: graphene, laminated composite materials, experimental testing, finite element, unmanned aerial vehicle.

1 Introduction

1.1 Motivation and Topic Overview

With less than two decades of being discovered, graphene is a material that can provide great properties enhancements in several fields of science and engineering. Its excellent electric and thermal conductive properties, as well as mechanical properties, are some examples that can be highlighted. Furthermore, it is the strongest material, making it a hundred to three hundred times stronger than most of the common steels. The Graphene Council (n.d.) states that combining graphene with other materials to form new hybrid ones has great benefits.

Graphene is a carbon-based material arranged in a two-dimensional honeycomb lattice (hexagonal) as can be seen in Figure 1. Its basic form naturally derives from graphite's delamination, and it consists of a thickness of one or a few several layers, which means a nanoscale dimension. Monolayer graphene represents one layer, and if more are stacked one obtains few-layer graphene for two to five layers. From six to ten layers one has multilayer graphene, and for more than ten layers it is called graphene nanoplatelets (Kumar, Kumar, Lee, & Park, 2021).

Considering its properties, graphene has great potential for application on aircraft structures. Nonetheless, there are still challenges to overcome before graphene can become a go-to solution. Papageorgiou, Kinloch, and Young (2017) allege

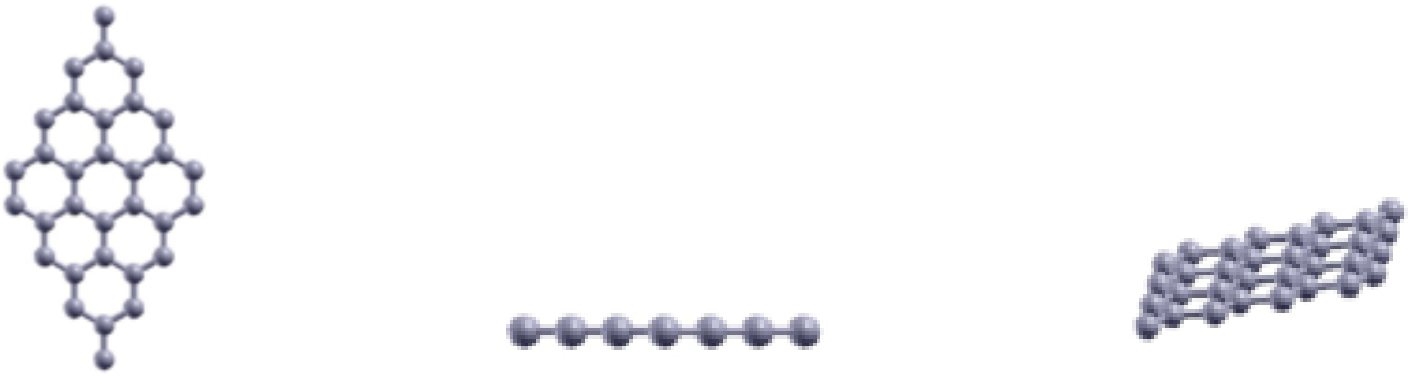

(a) Graphene top view (b) Graphene side view (c) Graphene perspective view

Figure 1: Graphene layer views. Retrieved from ISO/TS 80004-13:2017 (2017).

that high-quality and well-defined graphene production on a large scale is still a difficult task to perform. Besides that, they also state the challenge to obtain graphene's great properties while producing adequate dispersions. Graphene can be used in different forms. In this work, graphene is manufactured and incorporated in an epoxy matrix, HexaMatrix by Graphenest, S.A., a Portuguese graphene-based solutions provider.

In order to study the effect of incorporating graphene on the composite matrix, extensive experimental work will be performed. This study will determine the stress values and mechanical properties of several specimens subjected to tensile and flexural tests. In order to compare with conventional composites, HexaMatrix will be compared with SR8200, which is the epoxy matrix currently used in the *Centro de Investigação da Academia da Força Aérea* (CIAFA), and with HexaMatrix neat resin (without graphene). All specimens will be manufactured with carbon fibers (CF) used in CIAFA by hand layup.

Once the mechanical properties have been investigated, a comparative study will be conducted to determine the impact of different resins on several aircraft structures. To achieve this goal, the wing structure and its main spar from Alves et al. (2021) Class I electric vertical take-off and landing (eVTOL) unmanned aerial vehicle (UAV), with a maximum take-off weight of 25 kg, will be designed using SR8200 and HexaMatrix resins.

1.2 Objectives

The main goal of this report is to evaluate the impact of graphene-based resin incorporation in the matrix of the laminated composite with carbon fibers. The study will have two main purposes:

- Evaluate the mechanical properties of laminated carbon composite specimens:
  - Build specimens containing three different resins by the hand layup method. SR8200 (currently in use in CIAFA), HexaMatrix neat resin, and HexaMatrix (with graphene);
  - Perform tensile and flexural tests using ISO standards;
  - Analyse the obtained results and conclude the final approximate mechanical properties of each laminated type;
  - Infer on the improvement of the mechanical properties due to the addition of graphene on the epoxy matrix.
- Study the impact of graphene on aircraft structure design:
  - Structural design of a UAV Class I main spar and wing, using the three resins;
  - Comparison of results and discussion of the impact graphene had on the structures.

The development of this study will be aided by some software. Either the design and the finite element analysis from the computational design of the wing will be held on Siemens NX. While the analysis of data and further calculations will be made in Excel spreadsheets.

2 Fundamental Concepts and State-of-the-Art

2.1 Graphene, a New Material

Graphene was first unambiguously produced and identified in 2004, by the group of Andre Geim and Konstantin Novoselov, though they credited Hanns-Peter Boehm and his co-workers for the experimental discovery of graphene in 1962, where Boehm introduced for the first time the term graphene in 1986 (Geim, 2012).

Professor Andre Geim and Konstantin Novoselov, at the time researchers at the University of Manchester, in the United Kingdom, applied a simple graphite peeling method. This was all achieved by just using simple adhesive tape, commonly known as the "Scotch Tape" technique, which is a micromechanical cleavage process. This method had to be applied repeatedly to get one atom thick layers and finally obtain isolated graphene ("This Month in Physics History: October 22, 2004: Discovery of Graphene", 2009). With this discovery, six years later, they were awarded the Nobel Prize in the field of physics.

There are several methods to synthesize graphene that can be divided into two groups. The first is top-down where macro components, such as graphite, can be reduced into smaller elements. The second is bottom-up where smaller

elements are built up until graphene is obtained. While the first can cost-effectively make greater amounts of graphene, the second group can only produce smaller quantities of higher-quality graphene with higher costs (Zhang, Fraser, Ye, Merle, & Barralet, 2019). Examples of techniques from the first group are mechanical exfoliation (used by Geim and Novoselov in the discovery of the material), liquid-phase exfoliation, and chemical oxidation-reduction. From the second group, one can highlight the chemical vapor deposition and the epitaxial growth.

In its structure, monolayer graphene is composed of just one single layer of carbon atoms, where each of them connects to three others through *sigma* bonds, which are the strongest of all covalent bonds. Several techniques are used for characterizing graphene and identifying functional groups and/or morphological modifications on the graphene sheets, where one can highlight the Raman spectroscopy and both transmission electron and atomic force microscopies as some of them (Fraga, Sobrinho, Carvalho, & Ghislandi, 2020).

Graphene's exceptional mechanical properties are due to the structure bonds' stability which withstands in-plane deformations (Papageorgiou et al., 2017). Stiffness and strength depend on several factors, such as if it is mono, few, or multilayer, its lateral size, crystallinity, and oxide reduction level. According to Lee, Wei, Kysar, and Hone (2008), graphene's elastic response to the uniaxial extension test led to a Young's modulus value (E) of 1.0 ± 0.1 TPa, and an intrinsic breaking strength value (σ_{int}) of 130 ± 10 GPa at a strain (ε_{int}) of 0.25.

Regarding graphene applications in aeronautical structures, it can be applied in two different ways. The first comprises the addition of graphene to the epoxy resin to improve the resin's mechanical properties. The second is graphene-reinforced carbon fibers, where strength and stiffness can both be enhanced compared to traditional carbon fibers (Rafiee, Nitzsche, Laliberte, Thibault, & Labrosse, 2019). In both methods, graphene allows the decrease of the structural weight.

Adding graphene to structures could also enable electrical signals to propagate through it, leading to the concept of smart structures. These could carry data signals while stress and strain could be measured during the flight due to this multifunctional properties of graphene. Besides graphene being incorporated in structural materials, it can also be present as an aircraft paint coating. Due to graphene's electrical properties, special coatings have been developed to bridge radar detection, decreasing aircraft radar cross-section and making it more stealth to enemy radars. They can reduce drag, be used in de-icing systems and provide lightning strike protection (Aerospace Technology Institute & The University of Manchester, 2018).

2.2 Laminated Composite Materials

A composite material comprises two or more materials to create one new material (Dorworth, Gardiner, & Mellema, 2009). Laminated composites are fiber reinforcements bonded together by a matrix material to form a stack of plies. The three most common types of fibers used on laminated composites are carbon, glass, and aramid fibers. Table 1 shows a summary of the material that will be used to manufacture the laminated composite specimens.

Table 1: Composites for the production of laminates.

Fibers	Bidirectional Carbon Fabric, 3K, High Strength (HS), Plain Weave, 160 g/m^2
	Unidirectional Carbon Tape, 6K, High Resistance (HR), 215 g/m^2
Resin 1	Sicomin SR 8200 + Hardener: SD 7206
Resin 2	Graphenest pristine HexaMatrix (no graphene)
Resin 3	Graphenest HexaMatrix

Several methods and techniques can be employed to manufacture laminated composites. Wet layup molding is the method chosen for the preparation of the specimens. Usually, the resin is impregnated into the fibers using a roller or a squeegee (see Figure 2(a)). The use of vacuum bagging enhances the quality of the final product by aiding the impregnation process and removing the epoxy resin excess from the produced composite laminates (see Figure 2(b)).

Through thorough testing based on ISO standards, specimens will be subjected to tensile and bending tests carried out at the laboratory in order to determine their mechanical properties.

For tensile specimens to be produced and tested, bidirectional and unidirectional carbon fiber specimens followed the ISO/DIS 527-4 (2020a) and ISO/DIS 527-5 (2020b) standards, respectively. Adding that glass fiber tabs will be bonded to the

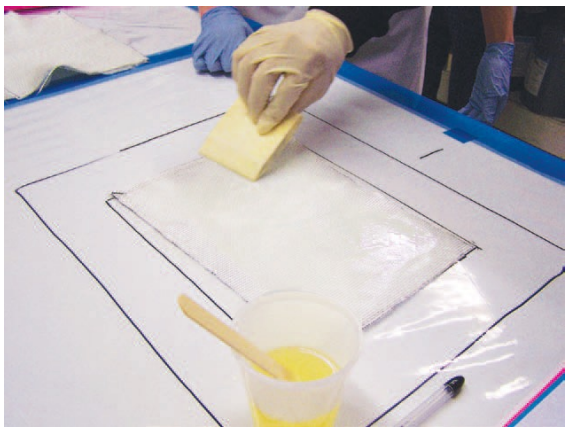

(a) Hand layup - Wet layup

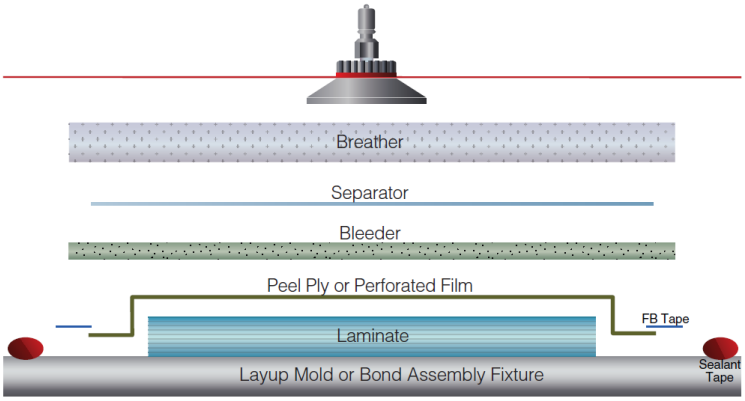

(b) Vacuum bagging

Figure 2: Production method. Retrieved from Dorworth et al. (2009).

specimen's ends, on both sides, to prevent specimens from breaking due to the pressure of the clamps. Flexural specimens will adopt ISO 14125:1998 + AC:2002 + A1:2011 (2011) for both types of carbon fibers used. Every standard recommends a minimum of five specimens per test condition. In order to obtain higher precision, a minimum of ten specimens per test condition are to be produced. Figure 3 presents the tensile test, and its respective tensile specimen, and the three-point flexural test.

Regarding the tensile test, through eq. (1) one can calculate de Young's modulus, where σ is the axial stress and ε is the specimen's strain due to the applied stress. Both can be obtained from eqs. (2) and (3), respectively, where F is the applied force, A is the specimen's cross-section area, and L_o is the specimen's gauge length. Δ represents the variables variation due to the applied load.

$$E = \Delta\sigma/\Delta\epsilon \qquad (1) \qquad \sigma = \frac{F}{A} \qquad (2) \qquad \varepsilon = \frac{\Delta L_0}{L_0} \qquad (3)$$

Concerning the flexural test, through eq. (4) one can calculate the flexural modulus (E_f), through the specimen's dimensions and the deflections (s) for flexural strains $\varepsilon_f = 0.0005$ and $\varepsilon_f = 0.0025$, and the corresponding applied force, directly obtained from the test results. L represents the specimen's test span, b_1 its width, and h the thickness. Flexural stress (σ_f) and flexural strain (ε_f) can be obtained from eqs. (5) and (6), respectively.

$$E_f = \frac{L^3}{4b_1h^3}\frac{\Delta F}{\Delta s} \qquad (4) \qquad \sigma_f = \frac{3FL}{2b_1h^2} \qquad (5) \qquad \varepsilon_f = \frac{6sh}{L^2} \qquad (6)$$

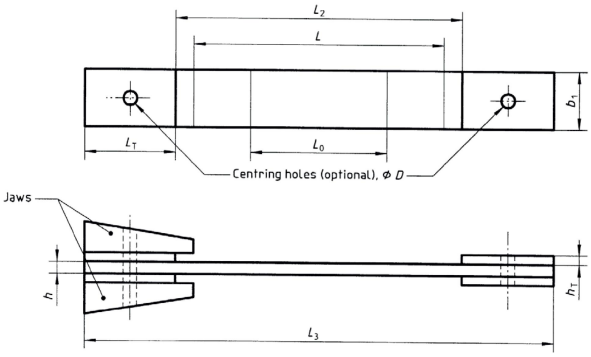

(a) Tension test specimen. Retrieved from ISO/DIS 527-4.

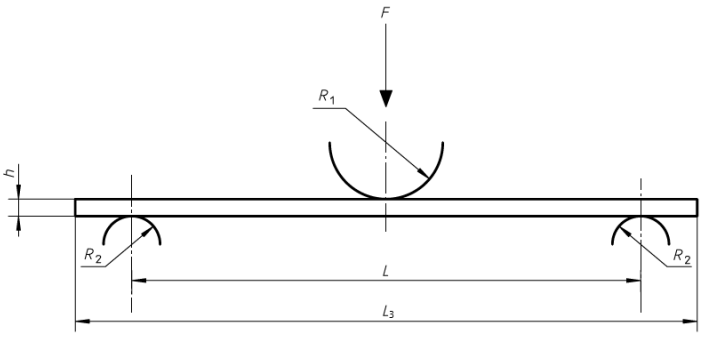

(b) Three-point flexural test. Retrieved from ISO 14125:1998 + AC:2002 + A1:2011.

Figure 3: Experimental tests diagrams.

2.3 Structural Analysis

Solid materials' mechanical properties follow stress-strain relations, which are called constitutive equations or constitutive relations. These equations characterize the applied load reaction of an individual material (Reddy, 2004). Furthermore, these equations are only applied to the material's elastic regime.

All the materials to be used in this work are orthotropic. Therefore, its constitutive relation is given by eq. (7), where E, G, and ν, included in the compliance matrix, are the Young's modulus, shear modulus, and the Poisson's ratio, respectively, for the direction/plane denoted by their subscript. Due to the symmetry in the compliance matrix, eq. (7) can be simplified by replacing the following entries from eq. (8) with their equal. Thereby, an orthotropic material only has nine independent components, which are the ones given by eq. (9).

$$\begin{Bmatrix} \varepsilon_{11} \\ \varepsilon_{22} \\ \varepsilon_{33} \\ 2\varepsilon_{23} \\ 2\varepsilon_{13} \\ 2\varepsilon_{12} \end{Bmatrix} = \begin{bmatrix} \frac{1}{E_1} & -\frac{\nu_{21}}{E_2} & -\frac{\nu_{31}}{E_3} & 0 & 0 & 0 \\ -\frac{\nu_{12}}{E_1} & \frac{1}{E_2} & -\frac{\nu_{32}}{E_3} & 0 & 0 & 0 \\ -\frac{\nu_{13}}{E_1} & -\frac{\nu_{23}}{E_2} & \frac{1}{E_3} & 0 & 0 & 0 \\ 0 & 0 & 0 & \frac{1}{G_{23}} & 0 & 0 \\ 0 & 0 & 0 & 0 & \frac{1}{G_{13}} & 0 \\ 0 & 0 & 0 & 0 & 0 & \frac{1}{G_{12}} \end{bmatrix} \begin{Bmatrix} \sigma_{11} \\ \sigma_{22} \\ \sigma_{33} \\ \sigma_{23} \\ \sigma_{13} \\ \sigma_{12} \end{Bmatrix} \quad (7)$$

$$\frac{\nu_{21}}{E_2} = \frac{\nu_{12}}{E_1}, \frac{\nu_{31}}{E_3} = \frac{\nu_{13}}{E_1}, \frac{\nu_{32}}{E_3} = \frac{\nu_{23}}{E_2} \quad (8)$$

$$E_1, E_2, E_3, G_{23}, G_{13}, G_{12}, \nu_{12}, \nu_{13}, \nu_{23} \quad (9)$$

In order to simplify the wing model analysis, instead of producing the structure and performing tests on it, one can previously design it using Computer-Aided Design (CAD) software and then simulate the applied loads to obtain the results. The Finite Element Method (FEM) is one of the numerical simulation methods that allow one to obtain approximate solutions of the real structure's response.

For the case of laminates, shell elements, which represent the 2D surface of the structure were chosen for the structure's mesh. Meshes are mainly composed of quadrilateral elements since greater accuracy can be achieved, while triangular elements have low usage.

Two different analyses will be performed on the UAV main spar and wing structures. The first will be a linear static analysis and the second a linear buckling analysis.

Linear Static Analysis In order to obtain stress and strain values due to an applied load, one can perform a linear static analysis. This assumes the geometric linearity hypothesis, where obtained results are linearly proportional to the applied loads. One can also obtain from this analysis the nodal displacements and rotations, and the constraint reaction's force and moment. A linear analysis is performed since only the elastic range of the materials is analysed and deformation is assumed to be small.

Linear Buckling Analysis This type of analysis is associated with compressive loads that lead to instability phenomena and consequential deformations. Linear buckling analysis does not assume a geometric linearity hypothesis. It allows to obtain the relative buckling loads. This parameter can be multiplied by all applied loads in the structure to obtain the buckling loads that lead to the structure's instability. For a relative buckling load lower than one, the structure will suffer from buckling effects. Different buckling deflection patterns can be obtained. This corresponds to the buckling modes of the structure, which are the eigenfunctions. Each buckling mode is induced by a specific buckling load, which are the eigenvalues of the problem (Simitses & Hodges, 2005). The lowest buckling load, which leads to the first buckling mode is usually called the critical buckling load.

3 Mechanical Properties - Specimen Experimental Tests

3.1 Preliminary Mass Calculations

To estimate the necessary resin, hardener and fiber mass quantities for the experimental part, initial calculations had to be performed based on theoretical equations from the laminates' rule of mixtures.

Carbon fiber mass density (ρ) was considered to be 1.80 $\times$ 10^3 kg/m^3 defined by (Toray Composite Materials America, 2018) for the T700G carbon fiber, a similar material to the one used in the experiment. The epoxy resin and hardener densities are listed in Table 2. From now on, each matrix will be referred to as Resin 1, 2, and 3, as presented in Table

1. The fiber and matrix volume ratios were 60/40%. As for the matrix mixture between the resin and the corresponding hardener, both weight and volume ratios are also presented in the Table 2.

Table 2: Epoxy resins and hardener's densities and mixing ratios.

	Resin Density [kg/m^3]	Hardener Density [kg/m^3]	Mix Weight Ratio	Mix Volume Ratio
Resin 1	1175 ± 10	1040 ± 10	100 g Res. - 37 g Hard.	100 mL Res. - 42 mL Hard.
Resin 2	1158	942	100 g Res. - 22 g Hard.	100 mL Res. - 27 mL Hard.
Resin 3	1158	942	100 g Res. - 22 g Hard.	100 mL Res. - 27 mL Hard.

Specimen sizes were extracted from the ISO standards defined in Section 2.2, and the panels to be produced were designed in accordance with the specimens' safety distances between each other and the panel's margins. The final total masses of fibers and epoxy resin and hardener are presented in Table 3.

Table 3: Theoretical total fiber, resin, and hardener mass.

	Total fiber mass [g]
Bidirectional Fibers	1156.68
Unidirectional Fibers	554.04
Glass Fibers	739.56

	Total resin mass [g]	Total hardener mass [g]
Resin 1	332.89	123.75
Resin 2	192.57	42.30
Resin 3	192.57	42.30

3.2 Laminate Specimen Manufacturing Process

During the production of the laminated panels, a matrix excess is necessary to compensate for its waste and to guarantee a good impregnation of the fibers. A CIAFA's experimental technique is to increase the mass of fiber by 10%. Then the obtained value will be multiplied by 1.5 to obtain the total matrix mass, leading to higher values of resin and hardener than the ones obtained in Table 3.

ISO standards mentioned in Section 2.2 requires the specimens for both flexural and bidirectional tensile to be 2 mm thick and the unidirectional tensile specimen to be 1 mm thick. After performing some preliminary testing, it was determined that ten plies were necessary to get a 2 mm bidirectional carbon laminate. As for the unidirectional carbon laminate, eight and four plies were required for the construction of flexural and tensile panels, respectively.

Epoxy matrix was applied to the dry fibers via the hand layup method (see Figure 4(a)). It the end, several films were added on top of the last ply, according to Figure 2(b), and the vacuum bag was closed for the curing process (see Figure 4(b)). After this process ends, post-curing was performed according to each matrix datasheet. Resin 1 post-cure process lasted for 10 days at room temperature (RT) of 23 ℃, while resins 2 and 3 took 24 hours at 40 ℃. Last, panels had to be cut on a Computer Numerical Control (CNC) Milling Machine in order to get each individual specimen (see Figure 4(c)). These were then sanded so that they were ready to be measured and then tested (see Figure 4(d)).

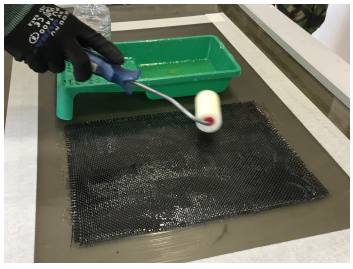

(a) Matrix application on a bidirectional carbon fabric.

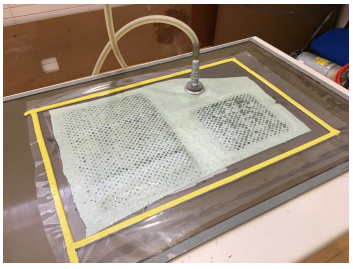

(b) Vacuum bag closed.

(c) CNC milling machine.

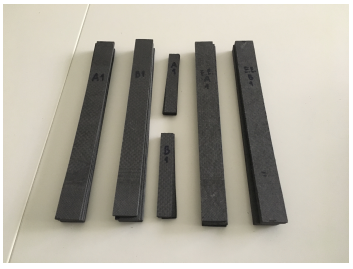

(d) Some specimens after being milled and sanded.

Figure 4: Laminates production phases.

3.3 Testing

First of all, each specimen's length, width, thickness, and weight were measured to obtain their fiber/matrix volume ratios. These ratios were important to compare if the production of the different materials was similar. Otherwise, another variable was being added to the study.

Tensile tests were run on the CIAFA's MTS Systems model 810 tensile testing machine with a 100 kN load cell. The test was configured and executed using the software TestWorks 4. This test was run at a strain rate of 2 mm/min.

It is worth mentioning that all bidirectional specimens broke in the center region (see Figure 5(a)). However, some also broke at the top and/or bottom, near the end tabs. This was due to the specimen's stress decompression after the first breakage. As for the unidirectional specimens, because transversal fibers are being connected with very thin glass fiber, these had a more aggressive breaking. Some of them totally shattered across a region. Others had groups of fibers breaking in different regions (see Figure 5(b)).

For flexural testing was estimated that a point load of magnitude of approximately 400 N was sufficient to break the specimen. Since the MTS 810 at CIAFA's facilities is equipped with a 100 kN load cell, sensitivity would have been very low, leading to an increased difficulty to obtain precise stress and strain values at break. Therefore, the flexural testing was performed at the IST's Mechanical Engineering Department, in Lisbon, using an Instron model 5566 testing equipment with a 500N load cell. A rate of displacement of 5 mm/min was set and the displacement and the applied force were obtained with a frequency of 50Hz.

In resemblance to the tensile test, the bidirectional specimens also broke at the center (see Figure 5(c)). As for the unidirectional, almost none had completely been broken into two pieces. The majority only broke several outer plies (see Figure 5(d)).

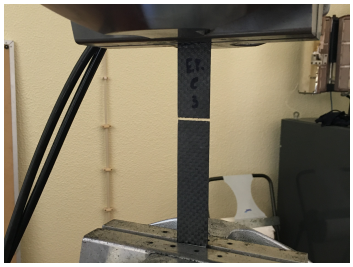

(a) Bidirectional specimen breaking at the center.

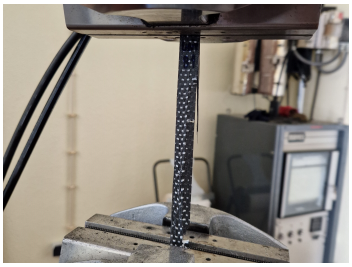

(b) Unidirectional specimen partially breaking.

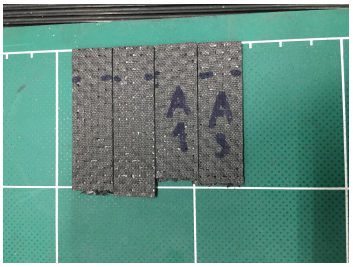

(c) Bidirectional specimens breaking at the center.

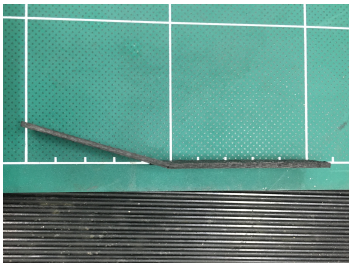

(d) Unidirectional specimen breaking several plies.

Figure 5: Specimens after being tested.

3.4 Results Analysis and Discussion

During the production and testing phases, several issues occurred: some panels had a low matrix volume ratio; the CNC milling machine cut some specimens out of the determined limits; and also, one end tab slipped out during the tensile test. All of these issues led to outliers. In order to eliminate undetected problems, an interquartile range method was applied to the mechanical properties, and to the obtained stress and strain values.

This interquartile range method seeks to calculate lower (LBound) and upper (UBound) boundaries for the specimens' results through eqs. (10) and (11). Primarily, the first (Q1) and third (Q3) quartiles were obtained for each test condition sample. Then, the interquartile range (IQR), which is the difference between these two values, was calculated.

$$LBound = Q1 - 1.5 \cdot IQR \tag{10}$$

$$UBound = Q3 + 1.5 \cdot IQR \tag{11}$$

It is worth mentioning that during tensile tests, some issues were detected:

- One specimen from the unidirectional resin's 1 third panel had its tabs slipping during the test;
- During the milling phase, four unidirectional resin's 2 specimens had a narrow cut;
- These and other specimens that were out of boundary limits were considered outliers and did not count for the mean values presented in the previews section. A total of 11 outliers out of the original 57 specimens were excluded.

For the flexural test, a total of 12 specimens out of 57 were considered outliers due to several issues:

- Bidirectional resin 1 batches were too thin. Most specimens were under the 1.8 mm thickness limit. Still, that difference was lower than 1% and the standard deviation was also low, so there were no outliers.
- For resin 2 and resin 3, thickness values were also low, but they did not cross the 1.8 mm lower bound limit.
- The unidirectional resin 3 had its third panel being produced with a very low matrix volume ratio, around 33%, as opposed to the other two panels which were 40.28%. This led to these three specimens' thicknesses crossing below the 1.8 mm limit. This third panel was considered an outlier.
- Panel production from resin 2 also presented the same problem. This time, the three panels were produced with a very low matrix volume ratio, leading to thin specimens that crossed the lower bound of 1.8 mm, leading to the complete disregard of the resin 2 unidirectional results.

According to the classical laminate theory, since the specimen's stacking is equal for each test specimen and all the plies are oriented at zero degrees, the Young's modulus should be the same as the flexural modulus. This statement is independent of the number of plies stacked. Table 4 show the modulus differences between Young's and flexural modulus results for bidirectional and unidirectional carbon fibers. The differences between the same modulus for different resins are shown in the last three columns of each table.

Table 4: Differences between Young's and flexural modulus results for bidirectional and unidirectional carbon fibers.

					Resins Differences [%]		
		Resin 1	**Resin 2**	**Resin 3**	**1 vs 2**	**2 vs 3**	**1 vs 3**
Bidirectional Carbon Fibers	**Young's Modulus [GPa]**	38.776	38.746	38.506	-0.1	-0.6	-0.7
	Flexural Modulus [GPa]	35.887	36.918	38.124	2.9	3.3	6.2
	Modulus Difference [%]	-7.4	-4.7	-1.0	-	-	-
Unidirectional Carbon Fibers	**Young's Modulus [GPa]**	83.664	82.204	82.227	-1.7	0.0	-1.7
	Flexural Modulus [GPa]	87.430	49.677	73.394	-43.2	47.7	-16.0
	Modulus Difference [%]	4.5	-39.6	-10.7	-	-	-

For the following part of this work, the numerical software requires the elastic modulus from each material to be considered as the Young's modulus. Since the test case was a wing structure, the loads applied to these structures are mainly of the flexural type. As such, flexural test loads were used as they were the ones that most closely matches the aerodynamic loads, and the flexural modulus was the one to be considered in the numerical part.

Due to the problems found on unidirectional flexural specimens from resin 2 and 3, an estimation for flexural modulus, thickness, and peak stress was performed following eq. (12). This way, unidirectional flexural modulus resins difference values from Table 4 will now be the same as the bidirectional ones. Due to time constrictions, more tests could not be performed on these materials in order to increase available data and results accuracy. Table 5 shows the final results for each resin.

$$Estimated\,Value\;for\;Resin\;X = \frac{Bidirectional\;Resin\;X}{Bidirectional\;Resin\;1} \times Unidirectional\;Resin\;1 \tag{12}$$

Table 5: Final material results to be used in the numerical solution.

		Resin 1		**Resin 2**		**Resin 3**	
		Bidirectional	**Unidirectional**	**Bidirectional**	**Unidirectional**	**Bidirectional**	**Unidirectional**
Ply Thickness [mm]		0.178	0.246	0.181	0.250*	0.183	0.252*
Mass Density [kg/m^3]		1518.7	1515.5	1492.1	1492.1	1493.5	1493.5
Area Density [g/m^2]		270.79	372.37	270.66	372.87	272.72	375.77
Young's Modulus [GPa]	**E_1**	35.887	87.430	36.918	89.943*	38.124	92.881*
	E_2	35.887	-	36.918	-	38.124	-
Ult. Tens. Streng. [MPa]	**UT_1**	664.82	926.54	661.54	921.98*	645.36	899.43*
	UT_2	664.82	-	661.54	-	645.36	-

* Estimated values using eq. (12)

4 UAV Wing Design

4.1 Baseline Design

In this section is addressed the design of a UAV wing using the materials characterized in the previous section. The wing baseline design that will be analysed is the main wing of the conceptual design of an eVTOL Class I UAV (Alves et al., 2021), represented in Figure 6. The UAV conceptual design resulted in a fixed-wing with an inverted V-tail configuration with a maximum take-off weight of 21.7 kg. For take-off and landing, four propeller electric engines are installed in two booms which connect the wing to the V-tail. An additional propeller electric engine is installed at the fuselage back end for fixed-wing flight. Sá (2021) has done the preliminary design of the main wing for this UAV, which is used as the baseline design to study the impact of including graphene in the composite matrix for aeronautical structures.

Figure 6: UAV conceptual design CAD model. Retrieved from Alves et al. (2021).

Figure 7 shows the CAD rendered image of the wing's baseline model design.

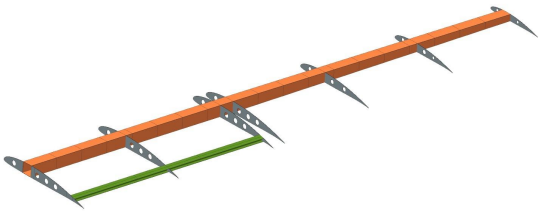

(a) Internal structure.

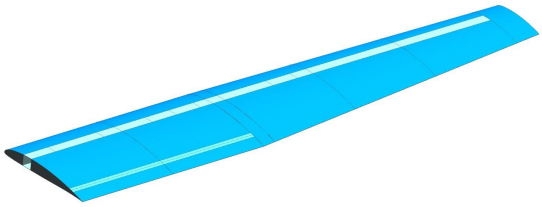

(b) External structure.

Figure 7: Wing's CAD model. Retrieved from Sá (2021).

The main spar has a rectangular cross-section with the dimensions presented in Table 6. To define the spar laminate, the spar's caps and webs were divided into nineteen 100 mm long sections. The spar design achieved by Sá (2021) is presented in Table 7. The base value represents the number of plies, and the exponent the number of sections having that number of plies. Caps were composed of unidirectional carbon fibers composite aligned with the span direction. Webs were composed of bidirectional carbon fibers at a 45º arrangement, where 0º is the span-wise direction. Both tables were retrieved from Sá (2021).

Table 6: Baseline spar dimensions.

Width	40 mm
Root Height	38 mm
Tip Height	20 mm
Span	1900 mm

Table 7: Baseline spar laminate distribution.

Top Cap	Lower Cap	Webs
5^1 / 4^3 / 3^3 / 2^4 / 1^8	5^1 / 4^2 / 3^3 / 2^4 / 1^9	2^5 / 1^{14}

Sá (2021) applied a distributed load along the spar's caps equal to the wing load for the ultimate load factor considered.

Concerning the wing, the main spar is at 33.5% of the wing's chord, where the airfoil thickness is maximum. The secondary spar is at 85% of the chord and it has a 750 mm length. Instead of a rectangular cross-section shape, it has an I shape, with a 20 mm cap width. The caps are composed of a unidirectional carbon fiber composite, with a laminate of two plies aligned with the span direction. The web is composed of a sandwich panel made of two bidirectional plies at a 45º arrangement with a core of 3 mm Airex C70.75 foam.

A total of seven ribs give the airfoil shape to the wing. Ribs 1 to 4 are composed of four bidirectional plies at a 45º arrangement with the chord-wise direction, and one unidirectional in the middle, perpendicular to the chord-wise. Ribs 5 to 7 have two bidirectional plies and one unidirectional in between, with the same respective alignment directions as the ribs previously mentioned. The wing tip has the same stacking. Finally, the skin is composed of two bidirectional plies at a 45º arrangement, where 0º is the span-wise direction.

A pressure load, equivalent to the aerodynamic load corresponding to the ultimate load factor, was applied to the wing skin.

4.2 Main Spar Design

The finite element analysis software requires the following material properties, in order to characterize an orthotropic material: mass density; Young's modulus in all three directions; Poisson's ratio in all three directions; and shear modulus in all three directions.

In Chapter 3, it was obtained the Young's modulus and ultimate strength of the 3 resins considered in the study. Therefore, it was necessary to use standard values for carbon fiber composites to fill in the materials' properties required by the software. The properties list was completed with data retrieved from a study done by Silva (2017). Table 8 presents the materials' properties used in the wing design.

Table 8: Material properties data set used in FEM analysis.

	Resin 1		**Resin 2**		**Resin 3**		
	Bi-Carbon	**Uni-Carbon**	**Bi-Carbon**	**Uni-Carbon**	**Bi-Carbon**	**Uni-Carbon**	**Airex + Epoxy**
Ply Thickness [mm]	0.178	0.246	0.181	0.250	0.183	0.252	3.000*
Mass Density [kg/m^3]	1518.7	1515.5	1492.1	1492.1	1493.5	1493.5	422.0*
E_1 [GPa]	35.887	87.430	36.918	89.943	38.124	92.881	0.066*
E_2 [GPa]	35.887	9.173*	36.918	9.173*	38.124	9.173*	0.066*
E_3 [GPa]	9.173*	9.173*	9.173*	9.173*	9.173*	9.173*	0.066*
ν_{12}	0.060*	0.262*	0.060*	0.262*	0.060*	0.262*	0.300*
ν_{13}	0.388*	0.262*	0.388*	0.262*	0.388*	0.262*	0.300*
ν_{23}	0.388*	0.396*	0.388*	0.396*	0.388*	0.396*	0.300*
G_{12} [GPa]	5.000*	5.000*	5.000*	5.000*	5.000*	5.000*	0.030*
G_{13} [GPa]	2.889*	5.000*	2.889*	5.000*	2.889*	5.000*	0.030*
G_{23} [GPa]	2.889*	3.470*	2.889*	3.470*	2.889*	3.470*	0.030*
UT_1 [MPa]	332.41	463.27	330.77	460.99	322.68	449.72	1.00*
UT_2 [MPa]	332.41	-	330.77	-	322.68	-	1.00*

* Values retrieved from Silva (2017)

The used methodology, either for the main spar analysis or the wing analysis, was to first perform, for both static and buckling analysis, a mesh refinement analysis. Then, after the converged mesh was chosen, results were analysed and verified if they agreed with the production and design safety parameters. If not, structural modifications were performed until a final design was met.

The main spar static analysis found two problems related to stress values in the spar's root corners and at the caps layer drop-offs. The first was stress singularities created due to the spar's fixed constraint that led to infinite stress as the mesh was refined. The second saw an unexpected stress increase on the caps plies decrease transition. Both problems did not affect the stress analysis, in order for it to comply with the materials' stress limits.

Regarding the main spar's results, static analysis proved that Sá's original design fulfilled the design requirements, while the buckling analysis revealed buckling phenomena on the top cap and webs. Thus, it had to be reinforced with more plies,

keeping up with the drop-off scheme. A complete ply, from root to tip, was also added due to the difficulty to produce one-ply laminates and the increased probability of buckling to occur. Adding that the webs were replaced with a sandwich panel with a core of 3mm Airex sheet plus two bidirectional outer plies since this was a lighter solution than the original one. Table 9 presents the laminate configuration of the lower and upper cap along the wingspan.

Table 9: Spar's model 2 laminate distribution after buckling analysis.

Top Cap	Lower Cap
7^3 / 6^3 / 5^4 / 4^3 / 3^3 / 2^3	6^1 / 5^2 / 4^3 / 3^4 / 2^9

Table 10 presents the final static and buckling analysis results for the three resins used and the corresponding difference between the value and the one from the resin 1 design. It is also presented the displacement relative percentage to the wingspan (2000 mm). Worst principal stresses were extracted to be compared with ultimate strength for failure purposes. Since it was not possible to implement any failure criteria on the software, this parameter is the most conservative regarding the stacking directions. It does not take into account failure due to shear stress.

Table 10: Final main spar's maximum displacement, stress and relative buckling load results comparison.

	Maximum Displacement			Lower Cap Max. Stress		Back Web Max. Stress		Mode 1	
	Displ. [mm]	Diff. [%]	Wingspan [%]	σ_{WP} [MPa]	Diff. [%]	σ_{WP} [MPa]	Diff. [%]	Relative Buck. Load	Diff. [%]
Resin 1	165.5	-	8.3	311.69	-	157.42	-	1.087	-
Resin 2	158.4	-4.2	7.9	306.89	-1.5	154.47	-1.9	1.154	6.2
Resin 3	152.6	-7.8	7.6	305.17	-2.1	153.10	-2.8	1.193	9.8

4.3 Wing Design

In this section, three main designs were obtained that henceforward will be named initial design, static design, and buckling design. The final design's, buckling design, performance is compared for the 3 matrix systems used in this work. Due to the results of the comparative study, two new designs are considered: first, it is proposed a wing structure configuration using components manufactured with resins 1 and 3; second, using these two resins in the manufacturing of the composite laminates, it is proposed a lighter design while fulfilling all requirements. For future reference, these designs will be named resin mix design and light design, respectively.

Initial Wing Design

As a first approach to the wing design, it was considered to include the spar model obtained in Section 4.2 in the wing baseline design (see Section 4.1). Linear static analysis shows that maximum stress is 41.5% lower than the ultimate design strength value given in Table 8. Buckling occurs in the wing skin as expected. However, the buckling load is 0.239, which means that the skin must be reinforced.

Although the wing structure fulfills all static requirements, the structure is oversized because the main spar's maximum stress is much lower than the allowed values. Therefore, this design is rejected and it is used Sá's wing design as the initial design for the static and buckling analysis. Sá's wing design has been validated for linear static load but it was not designed for buckling load.

Static and Buckling Designs

These designs will consider the final structure design at the end of each analysis. The buckling design will consider data from the static analysis and respective design.

The linear static analysis showed that the baseline design from Sá was in accordance with the requirements. Still, the skin panels close to rib 2 revealed convex deformations on the top skin and concave deformations on the bottom skin. These were then reinforced with plies keeping with the layer drop-off scheme. Stress singularities and discontinuities were once again found, but their results did not affect the structural integrity related to the laminate failure.

The linear buckling analysis showed deformations on the main spar's webs and on the top side skin panel between spars. These were both reinforced with a drop-off scheme until the relative buckling factor was higher than one. The top-side skin panel lay-up scheme is indicated in Table 11. As for the webs from both spars, these were tested with the layer

drop-off and with the sandwich foam core, where the first showed to be the most effective and the lightest of both. Spar's caps and ribs were kept unchanged from the baseline design from Sá.

Table 11: Buckling design - lay-up scheme.

Number of Plies	8	7	6	5	4	3	2
y-axis Position [mm]	0 - 100	100 - 500	500 - 750	750 - 1250	1250 - 1500	1500 - 1750	1750 - 2000

Resin Mix and Light Designs

In order to reduce the relative buckling load to 1 while keeping maximum stress lower than the allowed values, the first modification performed was to mix resin 1 and 3 in the same model. To that end, it is identified the components that had lower stress values with resin 1. It was decided to use resin 3 in the wing structure with the exception of the ribs and the wing tip which will be made of resin 1. This new design is called resin mix design henceforward.

The light design has the resin mixture from the resin mix design, while some plies are removed. The main goal is to reduce the number of plies from parts subjected to buckling because the behavior of the structure to buckling improved with the use of resin 3. Therefore, there is room to get a lighter structure while fulfilling the buckling criteria. The structural components considered in the study were the top skin panel, between the main and secondary spar, and the main spar top cap. There will be a trade-off between the relative buckling load decrease and the increase of the displacement.

An iterative process was performed to obtain a new ply configuration. The best solution achieved had some plies removed from the skin panels. It was not possible to remove material from the main spar top cap. The new configuration for the skin panel between spars laminate zones is presented in Table 12. The structural weight is estimated to reduce 43.3 g. Besides that, the manufacturing cost of the wing is also reduced because it requires less resin and fibers.

Table 12: Light design - lay-up scheme.

Number of Plies	7	6	5	4	3	2
y-axis Position [mm]	0 - 500	500 - 750	750 - 1000	1000 - 1250	1250 - 1500	1500 - 2000

Table 13 presents the main results for the buckling (resin 1, 2, and 3), resin mix, and light designs. The resin mix and light designs comparative values are relative to the buckling design with resin 3 values while buckling design with resin 2 and 3 are compared with the same design with resin 1. The bidirectional ply laminate's maximum stress was achieved for the outer ply from the top side skin panel between spars, close to the main spar root. The unidirectional maximum stress occurred for the adjacent point from the bidirectional maximum stress, corresponding to the unidirectional outermost ply.

Table 13: Final wing's maximum displacement, stress and relative buckling load results comparison.

	Maximum Displacement			**Bidirectional Max. Stress**		**Unidirectional Max. Stress**		**Mode 1**	
Model	**Displ. [mm]**	**Diff. [%]**	**Wingspan [%]**	σ_{WP} **[MPa]**	**Diff. [%]**	σ_{WP} **[MPa]**	**Diff. [%]**	**Relative Buck. Load**	**Diff. [%]**
Resin 1	112.1	-	5.6	-199.85	-	-431.22	-	1.014	-
Resin 2	108.2	-3.5	5.4	-194.88	-2.5	-423.80	-1.7	1.083	6.8
Resin 3	105.3	-6.1	5.3	-191.94	-4.0	-420.78	-2.4	1.126	11.1
Mix	105.3	0.0	5.3	-192.85	0.5	-420.63	-0.0	1.125	-0.1
Light	106.6	1.2	5.3	-190.41	-0.8	-407.95	-3.0	1.054	-6.4

To conclude, the light model is to be chosen as the final UAV wing model. It uses both resins in order to reduce weight and costs. The reduced number of plies from this model also allowed for a considerable weight decrease, considering it was only derived from changing the epoxy matrix, from resin 1 to resin 3, in almost all the structure.

The final wing design is comprised of: main and secondary spars made of resin 3 with the baseline configuration for the caps, and webs being made of four bidirectional plies; a top side skin panel between spars with a monolithic resin 3 laminate of bidirectional carbon fiber plies at 45º with a drop-off scheme as depicted in Table 12; the original ribs from the baseline design made of resin 1.

5 Conclusions

This work aimed to achieve two main objectives. The first was to characterize laminated composite materials made of three distinct matrices, through experimental tensile and flexural tests, in order to evaluate the impact of graphene on the mechanical properties of laminates. The second was to analyse the impact of graphene on the mechanical performance of two aeronautical structures by applying the properties obtained in the first part. The aeronautical structures were subject to static and buckling analyses and structural modifications were applied to meet the design requirements determined by standards.

Carbon fibers were the only common component in the laminated composite materials. The aim of the comparison study stood around the epoxy matrices which were different. Graphene nanoplatelets at a 2 wt% were incorporated in HexaMatrix produced by Graphenest S.A.. The other two were neat HexaMatrix and Sicomin SR 8200 with hardener SD 7206, currently used by CIAFA.

The experimental part of the work revealed the importance of composite laminate production on its mechanical properties. The amount of matrix applied to the fibers led to production issues, as was noticed for the unidirectional flexural resin 2 and 3 specimens. The tests results showed that graphene did not affect the specimen's tensile properties, since the results differences between the 3 resins for the two types of fibers were not significant.

As for the flexural modulus, bidirectional specimens presented a 3.3% increase between resin 1 and 2. For the graphene resin, this property improved by 6.2%. Due to the unidirectional issues above mentioned, their variations were tremendous when compared to the bidirectional specimens. These results were not coherent with the bidirectional ones, thus being eliminated from this study. Mechanical properties for the defective unidirectional specimens were estimated by having the same variations between matrices of bidirectional specimens. These were the ones mentioned at the beginning of the paragraph.

In the numerical simulation, the mechanical properties obtained in tensile and bending tests were complemented with mechanical properties values from previous tests of similar materials and from literature (Silva, 2017).

As a starting point for the numerical simulation, it was used the wing structure design obtained by Sá (2021), as the baseline design. The above-mentioned analyses were first performed on the main spar, and several structural modifications were performed after the original suffered from buckling deformations on the top cap and webs.

The use of HexaMatrix in the design of the main spar in spite of epoxy system SR8200 with hardener SD7206 allowed the following improvements:

- displacement decrease of 7.8%;
- critical buckling load increase of 9.8%;
- stress decrease between 2.1% and 2.8%.

The same analyses were made to the wing structure, which led to modifications in the spar's webs and on the skin panels. An initial wing design, including the final main spar design model, was oversized because the main spar's maximum stress was much lower than the allowed values. Therefore, this design is rejected and it was used Sá's wing design as the initial design for the static and buckling analysis, where structural modifications were performed to the main spar's webs and to the top side skin panel between spars.

The wing model presented similar improvements to the main spar when comparing the same two epoxy systems:

- displacement decrease of 6.1%;
- critical buckling load increase of 11.1%;
- stress decrease between 2.4% (unidirectional max. stress) and 4.0% (bidirectional max. stress).

To take advantage of the graphene properties, two different wing structures were designed. The first was called the resin mix design and it mixed components manufactured using both resin 1 and 3. The second was built upon the resin mix design and sought a decrease in the wing weight by decreasing the number of plies used in the top side skin panel while fulfilling static and buckling requirements. It was called light design and was considered the final wing model design of this work. A trade-off between the displacement increase and the weight and buckling load decrease was analysed to guarantee that design safety requirements continued to be fulfilled.

Comparing results from the light design with the ones from the resin 3 buckling design, there was a:

- displacement increase of 1.2%;

- critical buckling load decrease of 6.4% and weight decrease of 43.3 g;
- stress decrease between 0.8% (bidirectional max. stress) and 3.0% (unidirectional max. stress).

References

Aerospace Technology Institute, & The University of Manchester. (2018). Graphene exploitation material applications in aerospace. *INSIGHT papers*(Issue 6).

Alves, B., Coelho, V., Silva, P., Marta, A., Afonso, F., Sá, P., & Caetano, J. (2021). Design of a hydrogen powered small electric fixed-wing uav with vtol capability. In *International conference on multidisciplinary design optimization of aerospace systems* (pp. 290–304).

Dorworth, L. C., Gardiner, G. L., & Mellema, G. M. (2009). *Essentials of advanced composite fabrication & repair, washington: Aviation supplies & academics*. Inc.

Fraga, T. J., Sobrinho, M. A. d. M., Carvalho, M. N., & Ghislandi, M. G. (2020). State of the art: Synthesis and characterization of functionalized graphene nanomaterials. *Nano Express*, *1*(2), 022002. doi: 10.1088/2632-959x/abb921

Geim, A. K. (2012). Graphene prehistory. *Physica Scripta*, *T146*, 014003. Retrieved from https://doi.org/10.1088/0031-8949/2012/t146/014003 doi: 10.1088/0031-8949/2012/t146/014003

International Organization for Standardization. (2011). Iso 14125:1998 + ac:2002 + a1:2011 - fibre-reinforced plastic composites — determination of flexural properties [Computer software manual].

International Organization for Standardization. (2017). ISO/TS 80004-13:2017(en) Nanotechnologies — Vocabulary — Part 13: Graphene and related two-dimensional (2D) materials. *Online Browsing Platform (OBP) - ISO*. Retrieved from https://www.iso.org/obp/ui/#iso:std:iso:ts:80004:-13:ed-1:v1:en

International Organization for Standardization. (2020a). Iso/dis 527-4 - plastics - determination of tensile properties - part 4: Test conditions for isotropic and orthotropic fibre-reinforced plastic composites [Computer software manual].

International Organization for Standardization. (2020b). Iso/dis 527-5 - plastics - determination of tensile properties - part 5: Test conditions for unidirectional fibre-reinforced plastic composites [Computer software manual].

Kumar, V., Kumar, A., Lee, D.-J., & Park, S.-S. (2021). Estimation of number of graphene layers using different methods: A focused review. *Materials*, *14*(16). Retrieved from https://www.mdpi.com/1996-1944/14/16/4590 doi: https://doi.org/10.3390/ma14164590

Lee, C., Wei, X., Kysar, J. W., & Hone, J. (2008). Measurement of the elastic properties and intrinsic strength of monolayer graphene. *Science*, *321*(5887), 385-388. Retrieved from https://www.science.org/doi/abs/10.1126/science.1157996 doi: 10.1126/science.1157996

Papageorgiou, D. G., Kinloch, I. A., & Young, R. J. (2017). Mechanical properties of graphene and graphene-based nanocomposites. *Progress in Materials Science*, *90*, 75-127. Retrieved from https://www.sciencedirect.com/science/article/pii/S0079642517300968 doi: https://doi.org/10.1016/j.pmatsci.2017.07.004

Rafiee, M., Nitzsche, F., Laliberte, J., Thibault, J., & Labrosse, M. R. (2019). Simultaneous reinforcement of matrix and fibers for enhancement of mechanical properties of graphene-modified laminated composites. *Polymer Composites*, *40*(S2), E1732-E1745. Retrieved from https://onlinelibrary.wiley.com/doi/abs/10.1002/pc.25137 doi: https://doi.org/10.1002/pc.25137

Reddy, J. N. (2004). *Mechanics of laminated composite plates and shells: Theory and analysis*. CRC Press.

Sá, P. (2021). *Projeto estrutural de um veículo aéreo não tripulado com uma célula de combustível de hidrogénio* (Unpublished master's thesis). Academia da Força Aérea.

Silva, J. (2017). *Design and optimization of a wing structure for a uas class i 145 kg* (Unpublished master's thesis). Portuguese Air Force Academy.

Simitses, G. J., & Hodges, D. H. (2005). *Fundamentals of structural stability*. Elsevier.

The Graphene Council. (n.d.). *What is graphene?* Retrieved from https://www.thegraphenecouncil.org/page/WhatIsGraphene

This Month in Physics History: October 22, 2004: Discovery of Graphene. (2009). *APS NEWS*, *18*(9), 2.

Toray Composite Materials America, I. (2018). T700g standard modulus carbon fiber (5th ed.) [Computer software manual].

Zhang, Z., Fraser, A., Ye, S., Merle, G., & Barralet, J. (2019). Top-down bottom-up graphene synthesis. *Nano Futures*, *3*(4), 042003. Retrieved from https://dx.doi.org/10.1088/2399-1984/ab4eff doi: 10.1088/2399-1984/ab4eff